Supporting Information

A novel P-block single metal-site Tin-Nitrogen-doped Carbon (Sn-N-C) Fuel Cell Cathode Catalyst for the Oxygen Reduction Reaction (ORR)

Fang Luo[1], Aaron Roy[2], Luca Silvioli[3,4], David A. Cullen[5], Andrea Zitolo[6], Moulay Tahar Sougrati[2], Ismail Can Oguz[2], Tzonka Mineva[2], Detre Teschner[7,8], Stephan Wagner[9], Ju Wen[1], Fabio Dionigi[1], Ulrike I. Kramm[9], Jan Rossmeisl[3*], Frédéric Jaouen[2*] and Peter Strasser[1*]

[1]*Department of Chemistry, The Electrochemical Energy, Catalysis and Material Science Laboratory, Chemical Engineering Division, Technical University Berlin, Straße des 17. Juni 124, 10623 Berlin, Germany.*

[2]*ICGM, Univ. Montpellier, CNRS, ENSCM, Montpellier, France.*

[3]*Nano-Science Center, Department of Chemistry, University Copenhagen, Universitetsparken 5, 2100 Copenhagen, Denmark.*

[4]*Seaborg Technologies, Titangade 11, 2200 Copenhagen, Denmark.*

[5]*Center for Nanophase Materials Sciences, Oak Ridge National Laboratory, Oak Ridge, TN 37831, UAS.*

[6]*Synchrotron SOLEIL, L'orme des Merisiers, BP 48 Saint Aubin, 91192 Gif-sur-Yvette, France;*

[7]*The Fritz-Haber-Institute der Max-Planck-Gesellschaft, Inorganic Chemistry-Electronic Structure Group, Berlin 14195, Germany.*

[8]*Department of Heterogeneous Reaction, Max-Planck-Institute for Chemical Energy Conversion, 45470 Mülheim an der Ruhr, 14195 Berlin, Germany.*

[9]*Department of Chemistry and Department of Materials and Earth Sciences, Graduate School of Excellence Energy Science and Engineering, Technical University Darmstadt, Otto-Berndt-Str. 3, 64287 Darmstadt, Germany.*

*To whom correspondence should be addressed:

*e-mail: pstrasser@tu-berlin.de; frederic.jaouen@umontpellier.fr; jan.rossmeisl@chem.ku.dk

Methods

Catalyst synthesis

FeNC and NiNC: Aniline (Sigma-Aldrich) was first dissolved in 0.5 M HCl solution. Thereafter, the metal precursor (2.43 g $FeCl_3$ or 1.41 $NiCl_2$) was added into the solution, which was kept stirred for 15 min to be fully mixed with aniline. After the complete dissolution/mixing of the metal precursor with aniline, ammonium peroxydisulfate (APS, $(NH_4)_2S_2O_8$, Sigma-Aldrich) was dissolved in the solution as oxidant to form polyaniline, followed by the addition of the activated ketjen-600 black carbon that had previously been pretreated with 0.5 M HCl and 67 % HNO_3. The polymer suspension was kept at room temperature until the equilibrium condition was reached. Carbon supported metal/PANI was refluxed for 5 hours at 80-90 °C and afterwards dried at 80 °C overnight by using an oil bath. The dried powder was ball milled and pyrolysed at 900 °C under nitrogen for 1 hour. After the first pyrolysis, one typical acid leaching step was used to remove all un-reacted metal species: the resulting catalyst powder was acid-washed with a 1 M H_2SO_4 for catalysts with $FeCl_3$ and $NiCl_2$ as precursors, a second pyrolysis step (900 °C /1 hour/N_2) was performed, and again acid leaching/washing/drying. Finally, the third pyrolysis (900 °C/3h/N_2) was performed to achieve the final catalysts.

SnNC: 2 ml aniline (Sigma-Aldrich) was first dissolved in 500 ml 0.5 M HCl solution. Thereafter, 5 g ammonium peroxydisulfate (APS, $(NH_4)_2S_2O_8$, Sigma-Aldrich) was added to the solution for *in situ* polymerization of aniline while the mixture was kept at room temperature. The polymer suspension was kept at low temperature as long as no color change was observed. The activated ketjen-600 black (0.4 g) was mixed with de-ionized water for 30 min, and then it was added with PANI under constant stirring for 48 h to achieve uniformly distributed Ketjen and PANI suspension. Carbon supported PANI was refluxed for 5 hours at 80-90°C and then dried at 80 °C overnight by using an oil bath. Then Tin(II) chloride dehydrate (2.49 g $SnCl_2{\cdot}2H_2O$, anhydrous, Sigma-Aldrich) was added to the subsequent dried N-C powder, and ball milling was performed for half hour. The collected powder was pyrolysed at 900 °C for 1 hour in N_2 (the temperature protocols started with blowing continuous nitrogen purging (at room temperature) for more than 3 hours. Afterwards, the sequence heating process was continued in the heating ramp of 5 °C min^{-1} to 900°C in nitrogen atmosphere, kept for 1 hour at 900°C and finally cooled down naturely to certain temperature under a nitrogen atmosphere. Then the powder was dispersed in 500 ml 4M

HCl and refluxed under N_2 atmosphere at 90 °C for 8 hours, as first time acid leaching. After the acid leaching, the samples were washed to neutralize and then dried. The acid leached powders went through a second heat-treatment at 900 °C for 1 h (2^{nd} pyrolysis) and again acid leaching/washing/drying. Finally, the third pyrolysis (900 °C/3h/N_2) was performed to achieve the final SnNC catalyst.

CuNC: 2 ml aniline (Sigma-Aldrich) was first dissolved in 500 ml 0.5 M HCl solution. Thereafter, 2.43g Cupper (II) chloride dehydrate ($CuCl_2 \cdot 2H_2O$, anhydrous, Sigma-Aldrich) was added into the solution and was kept stirred for 15 min to be fully mixed with aniline. After the complete dissolution/mixing of metal and aniline, 5 g ammonium peroxydisulfate (APS, $(NH_4)_2S_2O_8$, Sigma-Aldrich) was added to the solution for *in situ* polymerization of aniline while the mixture was kept at room temperature. The polymer suspension was kept at low temperature as long as no color change was observed. The activated ketjen-600 black (0.4 g) was mixed with de-ionized water for 30mins, and then added with metal/PANI under constant stirring for 48 hours to achieve uniformly distributed Ketjen and PANI suspension. Carbon supported metal/PANI was refluxed for 5 hours at 80-90°C and then dried at 80 °C overnight by using an oil bath. The subsequent dried powder was grinded byball milling and pyrolysed at 900 °C for 1 h in N_2 (flowing N_2 through the quartz tube under room temperature for 2 hours, then 5 °C/min temperature rate for heating up to 900 °C, holding 1 hour under N_2, then cooling overnight under N_2). Then the powder was dispersed in 500 ml 2M HNO_3 and refluxed under N_2 atmosphere at 90 °C for 8 hours as first time acid leaching. After the acid leaching, the samples were washed to neutralize and then dried. The acid leached powders went through a second heat-treatment at 900 °C for 1 hour (2nd pyrolysis) and again acid leaching (2M HNO_3/7-8h, 80-90°C) /washing/drying. Finally, the third pyrolysis (900 °C/3h/N_2) was performed to achieve the final CuNC catalyst.

CoNC: 0.8 g of a Zn(II) zeolitic imidazolate framework (ZIF-8, Sigma Aldrich) and 0.2 g of 1,10-phenanthroline were weighed, poured into a ZrO_2 crucible, followed by adding cobalt(II) acetate, with the mass of cobalt acetate corresponding to 0.5 wt.% of cobalt to the total mass of ZIF-8, phenanthroline and cobalt acetate. Then, one-hundred zirconium-oxide balls of 5 mm diameter were added and the ZrO_2 crucible was sealed under air. The precursors were homogenized in a planetary ball-miller (Fritsch Pulverisette 7 Premium, Fritsch, Idar-Oberstein, Germany) with 4 cycles of 30 min at 400 rpm. The resulting catalyst precursor was flash-pyrolyzed at 1050 °C in

Ar flow for 1 h. The pyrolysis was stopped by opening the split hinge oven, removing the quartz tube and letting cool down the catalyst under Ar flow.

N-C: 2ml Aniline (Sigma-Aldrich) was first dissolved in 0.5 M HCl solution, 5g ammonium peroxydisulfate (APS, $(NH4)_2S_2O_8$, Sigma-Aldrich) was dissolved in the solution as oxidant to form polyaniline, followed by the addition of the 0.4 g activated ketjen-600 black carbon that had previously been pretreated with 0.5 M HCl and 67 % HNO_3. Carbon supported PANI was refluxed for 5 hours at 80-90 °C and afterwards dried at 80 °C overnight by using an oil bath. The dried powder was ball milled and pyrolysed at 900 °C under nitrogen for 3 hours. After the first pyrolysis, the resulting catalyst powder was acid-washed with 1 M H_2SO_4 for 8 hours. A second pyrolysis step (900 °C /1 hour/N_2) was performed to achieve the final catalysts.

NH_3 Activation: SnNC, FeNC, and CoNC were further activated by loading 100–200 mg of pristine catalyst into a tubular furnace. The flow rate of anhydrous NH_3 was maintained at ~200 sccm for 2 hours while the furnace was allowed to equilibrate at the activation temperature of 750 or 900℃, with the catalyst powder outside of the heating zone. The activation temperature was optimized for each catalyst, to give the highest PEMFC performance. Once the oven had equilibrated at the set temperature (i.e. 2 h of equilibration once the temperature indicator reached the set temperature), the catalyst powder was inserted in ca 30 s in the heating zone with an outer magnet, by pushing a quartz rod/magnet assembly, previously installed inside the quartz tube. The NH_3 activation was carried out for 5 min, and the split hinge furnace was then opened and quartz tube removed to quench the temperature and stop the NH_3 activation. This flash pyrolysis process is fully described in Ref[1].

Physical characterization

Elemental Analysis was performed with a Thermo Electron, Flash EA 1112 analyzer. N_2-physisorption measurements were performed on an Autosorb-1-C from Quantachrome Company. The tubes were filled with catalyst powder and degassed by heating for 24 h at 60 °C under vacuum. Subsequently, the sample was cooled down with liquid nitrogen and the N_2 adsorption and desorption isotherms recorded. The BET-specific surface area and pore size distribution were then calculated with the Quantachrome software (DFT model). Bulk metal contents were measured

with ICP-OES on a Varian 715-ES. A known amount of sample was digested in a mixture of 2 mL sulfuric (98 wt%), 2 mL nitric (69 wt%), and 6 mL chloridric (37 wt.%) acids in a Microwave (CEM SP-D Discover) until the solution became transparent. Cu Kα XRD was recorded by a D8 Advanced X-ray diffractometer from Bruker AXS (tube settings fixed at 40 kV and 40 mA), equipped with a position sensitive LynxEye detector (PSD). XPS and soft X-ray absorption spectroscopy at the iron L-edge were performed at the Innovative Station for In Situ Spectroscopy (ISISS) beamline of BESSY II of the Helmholtz-Zentrum Berlin at RT and under ultra-high vacuum conditions[2]. The Fe L-edge spectra were recorded in the total electron yield mode detected with a Faraday cup. N1s spectra were recorded with 950 eV excitation energy and were fit with eight Gauss-Lorenz (FWHM: 1.6±0.05eV, GL ratio: 0.65) and Gauss convoluted Doniach-Sunjic (FWHM: 1.45±0.05eV) functions after testing various combinations of fit parameters (peaks 1-8). The eight peak functions were then clustered into 4 binding energy (BE) ranges and denoted as BE-range 1-4. BE-range 1 includes Peak 1 (398.1 eV) and Peak 2 (398.7 eV) covering N bonded with 2 sp^2 carbon atoms and -C=N-C double bond motifs (e.g. Imine N, Pyridinic N, or triazinic N). BE-range 2 includes Peak 3 (399.3 eV) and Peak 4 (399.8 eV) covering sp^2 hybridized N in Metal-N coordination, OC-NH-C partial double bonds, or multiple graphitic N motifs in a single aromatic ring (e.g. M – Nx, Amides). BE-range 3 includes Peak 5 (400.7 eV), Peak 6 (401.8 eV), and Peak 7 (403 eV) covering hybridized N bonded with 1 H (in-place hydrogenated N), isolated graphitic N, out-of-plane hydrogenated/protonated N, and hydrogenated graphitic N (e.g. pyrrolic or protonated pyridinic, protonated graphitic N). BE-range 4 includes Peak 8 (405 eV) covering oxidized N (e.g. C=N-O or other oxidized N). The Gauss convoluted Doniach-Sunjic function was employed for peak 5 (400.7 eV), peak 6 (~401.8 eV), peak 7 (~403.0 eV) to account for the asymmetry on the high binding energy side of the major spectral peak. TEM on FeNC and SnNC was performed using a FEI Tecnai G2 20 S-TWIN with LaB_6-cathode, 200 kV accelerating voltage and a resolution limit of 0.24 nm. The samples were dispersed on a 200 mesh Cupper grid. Atomic-resolution images of atomically-dispersed Sn sites in SnNC were captured by aberration-corrected scanning transmission electron microscopy (STEM) using a Nion UltraSTEM 100 operated at 60 kV and equipped with a Gatan Enfina electron energy loss spectrometer. Aberration-corrected STEM images were acquired using a high-angle annular dark-field (HAADF) detector with a 54-200 mrad collection semi-angle at Oak Ridge National Laboratory. Mössbauer spectroscopy measurements were acquired on SnNC and FeNC in transmission mode at room temperature, and

the spectra fitted with appropriate combination of Lorentzian profiles by least-square methods. For ^{57}Fe Mössbauer spectroscopy, a CMCA-550 (Wissel) equipped with a constant electronic drive system, triangular reference wave form (Halder Electronics) and 3.7 GBq ^{57}Co/Rh source was used. The velocity scale and isomer shift δ_{iso} were calibrated with an α-Fe foil (25 μm thick, 99.99 % purity) in a velocity range of ± 8 mm s^{-1}. For measurement on FeNC, the catalyst powder was filled in PTFE sample holder and closed with TESA tape. Spectra analyses were done with MossWinn 4.0i. ^{119}Sn Mössbauer spectra were recorded in the constant acceleration mode. The Ca^{119m}SnO$_3$ source (with an activity of 10 mCi) and the absorber were both kept at 300 K in all experiments. The velocity scale was calibrated with the magnetically split sextet spectrum of a high-purity α-Fe foil as the reference absorber, using a ^{57}Co/Rh source. The spectra of the starting composite materials were fitted to appropriate combination of Lorentzian profiles by least-squares methods using the program Isofit. In this way, spectral parameters such as quadrupole splitting (QS), isomer shift (IS), linewidth (Γ) and relative resonance areas of the different spectral components were determined.

XAS measurements were carried out at room temperature in transmission geometry at the SAMBA beamline (Synchrotron SOLEIL). The energy was monochromatized by means of a sagittally bent Si 220 double crystal monochromator, and two Pd-coated collimating/focusing mirrors were used to remove X-ray harmonics. The catalysts were pelletized as disks of 10 mm diameter using boron nitride as a binder. The EXAFS data analysis was performed with the GNXAS code[3, 4]. The EXAFS χ(k) signal is decomposed into a summation over n-body distribution functions $\gamma^{(n)}$ calculated by means of the multiple-scattering (MS) theory, and depending on four parameters, namely, the coordination number N, the average distance R, the mean-square variation σ^2, and the skewness β. Each signal has been calculated in the Muffin-tin (MT) approximation using the Hedin-Lundqvist (HL) energy dependent exchange and correlation potential model, which includes inelastic loss effects. The SnNC theoretical spectrum have been modelled including the first shell Sn-N(C) and Sn-O $\gamma^{(2)}$ two body signals, and two Sn-C and Sn-Sn $\gamma^{(2)}$ two body signals. The $\gamma^{(3)}$ signal associated with the N(C)-Sn-N(C) three-body distributions has also been included. Least-square fits of the EXAFS raw experimental data have been performed by minimizing a residual function of the type:

$$R_i(\{\lambda\}) = \sum_{i=1}^{N} \frac{[\alpha_{\exp(E_i)} - \alpha_{mod}(E_i; \lambda_1, \lambda_2, \ldots, \lambda_p)]^2}{\sigma_i^2} \quad (1)$$

where N is the number of experimental points, Ei $\{\lambda\} = (\lambda 1, \lambda 2, \ldots, \lambda p)$ are the p parameters to be refined and σ_i^2 is the variance associated with each experimental point $\alpha_{exp}(E_i)$. Additional non-structural parameters were minimized, namely E_0 (core ionization threshold energy) and the many body amplitude reduction factor S_0^2.

CO Pulse Chemisorption

CO pulse chemisorption experiments were performed using a Thermo Scientific TPD/R/O 1110 instrument (setup illustrated in Figure S1 of Ref[5]) under a 20 ml min^{-1} flow of helium as carrier gas. 100-150 mg of catalyst was filled in a U-shaped quartz reactor and underwent the following three-step analysis. (i) a cleaning treatment involving heating the sample to 600 °C with a ramp rate of 10 °C min^{-1} under 20 sccm flow of 5 N helium, followed by a hold of 15 min at 600 °C and then by subsequent convective cooling back to room temperature. (ii) cooling of the cleaned catalyst to -80 °C, using a mixture of dry ice and acetone, followed by six consecutives 0.338 mL CO pulses, dosed at 25 min intervals, which were passed through the catalyst samples. The amount of CO retained in the catalyst was quantified using a TCD detector. (iii) a temperature-programmed CO desorption (TPD) was performed by ramping the temperature from -80 °C up to 600 °C with a ramp rate of 10 °C min^{-1} under 20 sccm flow of 5 N helium. The CO uptake was then normalized to the analyzed mass of the catalyst (n_{CO}, in mol_{CO} g^{-1}), and the site density per mass of catalyst (SD_{mass}) was then obtained from n_{CO} from the following equation:

$$SD_{mass}[sites\ g^{-1}] = n_{CO}[mol\ g^{-1}] \times N_A \quad (2)$$

Where N_A is Avogadro's number.

Electrochemical Measurements of ORR Activity and Selectivity

Electrochemical characterisation in a RRDE setup

Rotation-Ring disk electrode (RRDE) measurements were performed to determine the ORR activity and selectivity of MNC catalysts in acidic liquid electrolyte. 15.7 mg catalyst powder, 750 µl de-ionized water, 190 µl ethanol and 60 µl Nafion (5 wt% solution in alcohol) were sonicated for 15 min in order to prepare inks. The aliquot of the ink necessary to reach a catalyst

loading of 800 μg·cm^{-2} was pipetted on the glassy carbon disk (0.2475 cm^2). A carbon rod and a reversible hydrogen electrode (RHE) were used as counter and reference electrodes, respectively. An O_2-saturated 0.1 M $HClO_4$ aqueous solution was used as electrolyte. The disk potential was scanned between 0 and 1.1 V vs. RHE at 5 mV·s^{-1} while the ring potential was fixed at 1.2 V vs RHE. The collection efficiency of the RRDE electrode used was 0.37 ± 0.01. For Stability tests (STA) up to 9,000 rectangular-wave potential cycle between 0.6 to 1.0 V vs RHE were performed in N_2-saturated electrolyte with 30 seconds holding at the initial potential of 0.6 V vs RHE. 6-second was selected as a cycle period with recording potential at 0.6 V vs RHE for 3 seconds as well as at 1.0 V vs RHE for another 3 seconds. All ORR activity and stability tests were performed at room temperature in 0.1M $HClO_4$ (pH 1). The sweep voltammetric RRDE data were first corrected for capacitive currents, followed by iR correction of the uncompensated electrolyzer resistance.

The kinetic current density (j_k), mass activity (j_m), Tafel slope (mV decade^{-1}) and hydrogen peroxide yield were obtained from RRDE measurements based on the following equations:

- Kinetic current density (j_k): j_k was deduced from the total Faradaic current density, j, and the diffusion-limited Faradaic current density, j_d, with the Koutecky-levich equation,:

$$\frac{1}{j_k} = \frac{1}{j} - \frac{1}{j_d} \qquad (3)$$

Where the diffusion limiting current density j_d was chosen at potential 0.2 V vs. RHE

- Mass activity (j_m): j_m was derived from j_k vas following:

$$j_m = \frac{j_k}{m_{catalyst}} \qquad (4)$$

Where $m_{catalyst}$ is the total catalyst loading on the glassy carbon disc (0.8 mg cm^{-2}). The mass activity is reported at 0.8 V vs. RHE for comparing SnNC, FeNC and CoNC and at 0.7 V vs. RHE for comparing all MNC catalysts.

- Hydrogen peroxide yield (%): The % H_2O_2 was calculated from the ring and disk current with the following equation:

$$H_2O_2\% = 200 \times \frac{I_R/N}{(|I_D| + I_R/N)} \qquad (5)$$

Where I_R is the ring current (mA), I_D is the disk current (mA), and N is the collection efficiency.

TOF calculation

$$j_m\left[A\ g_{catalyst}^{-1}\right] = TOF[electrons\ site^{-1}\ s^{-1}] \times SD_{mass}\left[sites\ g_{catalyst}^{-1}\right] \times e[C\ electrons^{-1}] \quad (6)$$

where TOF is the turnover frequency, SD_{mass} is the mass-normalized site density, e is the electric charge of one electron.

DFT calculation of quadrupole splitting values for SnN_x sites in ^{119}Sn Mössbauer spectra

The QS values were computed similarly to our recent combined experimental and theoretical study on FeN_x sites[6], using the *ab initio* pseudopotential projector-augmented wave DFT method as implemented in the Vienna *ab initio* simulation package (VASP). The spin-polarized generalized gradient approximation with Perdew−Burke−Ernzerhof parametrization (GGA-PBE) was used for the exchange-correlation functional. For the calculation of structural and electronic properties, standard PAW potentials supplied with VASP were used, with 4 valence electrons for C ($2s^2\ 2p^2$), 5 valence electrons for N ($2s^2\ 2p^3$), 14 valence electrons for Sn ($5s^2\ 4d^{10}\ 5p^2$) and 6 valence electrons for O ($2s^2\ 2p^4$). When calculating electric field gradient, we have used the corresponding GW potentials, which give a better description of high-energy unoccupied states. Structural relaxation is performed with a convergence criteria of 1×10^{-2} eV/Å on force and a Γ-centered k-point grid of 8x8x1.Electron self-consistency loop is performed with a convergence criteria of 1×10^{-6} eV for total energy and a Fermi-Dirac smearing of 0.03 eV for electron. In addition, all the calculations included support grid for the evaluation of the augmentation charges.

The quadrupole splitting energy is computed as the coupling between the nuclear quadrupole moment (Q) the non-spherical nucleus and the principle components V_{ii} (i=x,y,z) of the electric field gradient (EDF) tensor at ^{119}Sn nucleus using the equation

$$\Delta E_Q = \frac{1}{2} eQV_{zz}\sqrt{1+\frac{\eta^2}{3}} \quad (7)$$

In the ΔE_Q equation, e is the charge of the electron and the asymmetry parameter η is computed as $= (V_{xx} - V_{yy})/V_{zz}$, where $|V_{zz}| \geq |V_{yy}| \geq |V_{xx}|$. The nuclear quadrupole moment, Q, for J=3/2 state is taken to be -132 millibarn. Computation of ΔE_Q and η therefore becomes a question of computing the EFG tensor, which is readily obtained as an expectation value of the EFG operator,

$V_{ij} = \langle \Psi_0 \left| \frac{3ij - r^2}{r^5} \right| \Psi_0 \rangle$, for the electronic ground state Ψ_0 and *i,j*=x,y,z being the components of the electron radius vector r. In the present study, the calculated value of ΔE_Q are reported in units of mm·s^{-1} (labelled as QS) for a direct comparison to experimentally reported values.

Supporting note

Supporting note 1. Discussion of the minor Sn-Sn back-scattering signal identified from EXAFS fitting

The EXAFS analysis finds a Sn-Sn bond distance of 3.28 Å with a coordination number of 1 averaged for all Sn atoms in the sample, which is consistent with the minor presence of nanosized SnO_2[7]. The presence of a small amount of SnO_2 (sub)-nanoclusters in the sample might have influenced the average coordination number for Sn-O in SnN_4 moieties. Specifically, the existence of Sn-O bonds, indicating the presence of a minor amount of SnO_2 clusters in the SnNC material, might have been fitted by an artificially increased average coordination number for Sn-O in the SnN_4 moieties.

Supporting note 2. Discussion of the possible reasons for the lower site density in SnNC vs. FeNC

The lower SD_{mass} value of SnNC vs. FeNC prepared nearly identically except for the different nature of the metal salts, may be due either to

i) The same weight % of Fe and Sn metals were used for preparing FeNC and SnNC (see Methods), naturally resulting in lower atomic % of Sn in the bulk of the N-doped carbon matrix relative to atomic % of Fe (due to twice higher atomic mass for Sn vs. Fe). Assuming that the ratio between the amount of metal sites located on the top surface and that located in the bulk of the N-doped carbon matrix is the same for SnNC and FeNC, the SD_{mass} value is expected to be circa twice higher for FeNC vs. SnNC.

ii) The hypothesis above (ratio of surface/bulk metal sites identical in both catalysts) may not be true, due to the lower specific area in SnNC vs. FeNC. Nitrogen sorption isotherms show indeed that SnNC has circa twice-lower microporous and BET surface areas compared to FeNC (**Figure S9**, **Table S7**). Assuming that a given maximum number of MN_x sites (independently on the nature of the metal) can form per unit surface area of carbon, then a lower SD_{mass} value of SnNC vs. FeNC can be explained simply due to the lower total specific area (and microporous area in particular) of the former per mass of catalyst.

Supporting note 3. Method for referencing theoretical and experimental volcano plot to Fe

While the x-axis position of the cross or circle symbols corresponding to each structure is given by its calculated G_{HO} value, their y-axis positions (for U on left y-axis) are adjusted by a constant value for all structures. The latter was determined by the vertical translation needed to position the U-value calculated for the FeN_4C_{10} structure exactly on the volcano line corresponding to 4e ORR. This in turn adjusts the right hand side scale of the y-axis (the U-value in the volcano line at the G_{HO} value calculated for FeN_4C_{10} is associated with the current measured for 4e ORR on FeNC). This "iron referencing" allows a direct visual proof-checking if calculated and experimental values fall on the Volcano lines for other metals, overcoming issues that may otherwise arise due to systematic errors in the DFT assumptions.

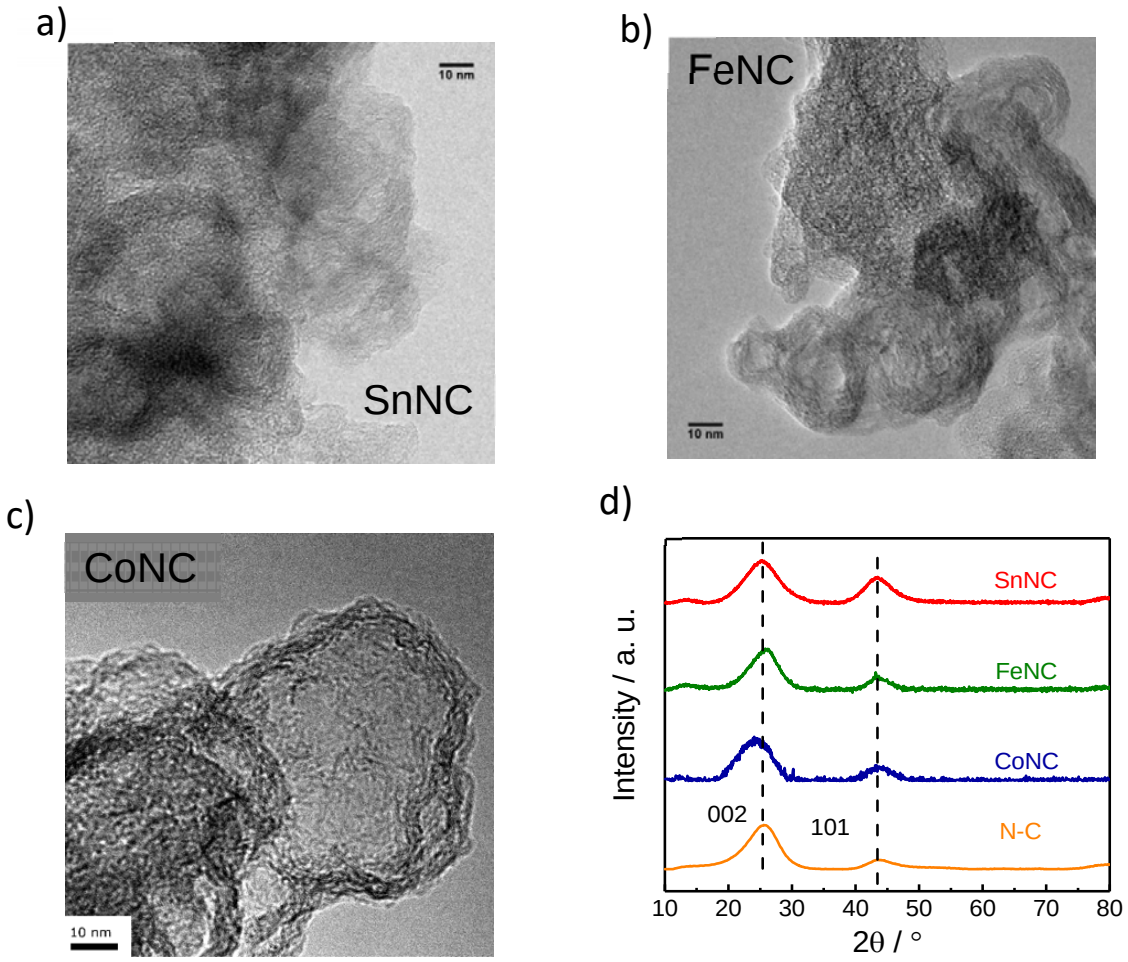

Figure S1. TEM images of (a) SnNC, (b) FeNC and (c) CoNC (reproduced from Figure S1e in Reference[8], with permission from Springer Nature), (d) XRD patterns of all three MNC catalysts and metal-free NC. The expected positions for the (002) and (101) reflections for graphite are indicated. The XRD patterns for SnNC, FeNC, and CoNC reveal only broad peaks assigned to nanometric graphitic domains, and no peaks for metal-rich crystallographic phases. NC was prepared identically to SnNC and FeNC, except for the omission of the metal precursor.

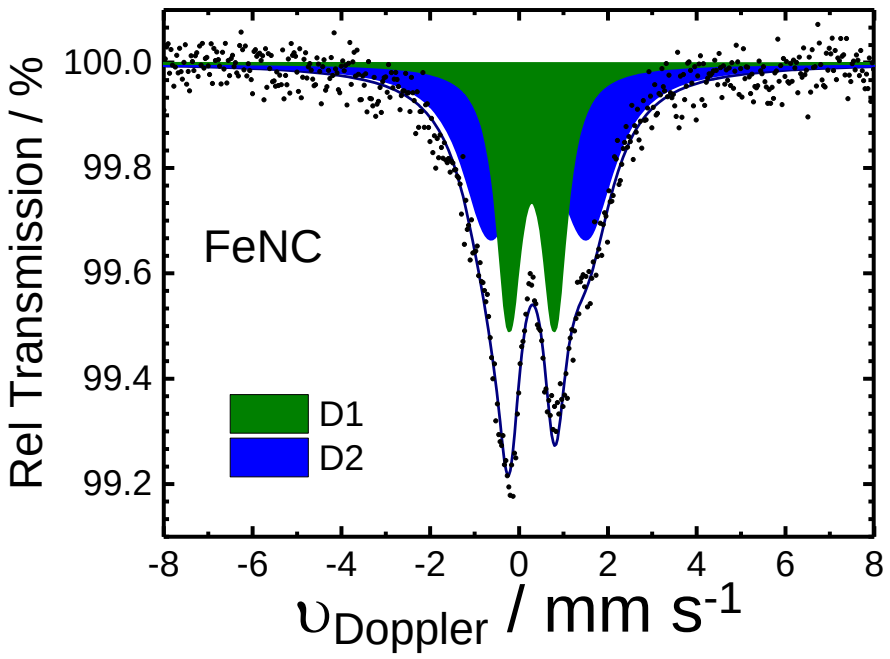

Figure S2. ^{57}Fe Mössbauer spectrum of FeNC and its fitting with two quadrupole doublets D1 and D2 assigned to FeN_4 moieties in different oxidation and spin states.

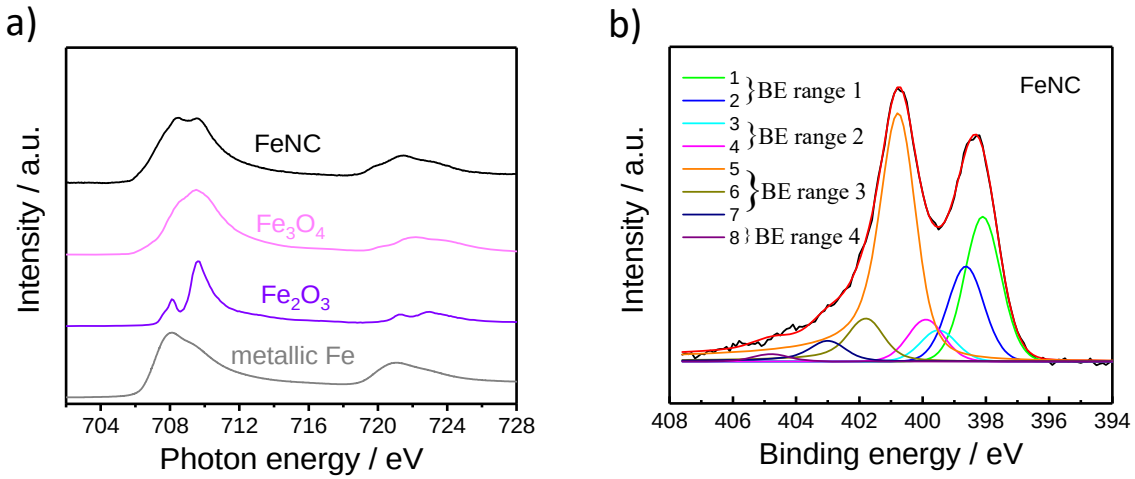

Figure S3. Characterization of Fe and N speciation in FeNC. (a) Normalized X-ray absorption spectra at the Fe $L_{3,2}$–edge for FeNC and reference compounds, (b) high-resolution N_{1s} XPS spectrum for FeNC. The Fe $L_{3,2}$–edge spectra for a metallic Fe foil, Fe_3O_4 and Fe_2O_3 are also presented to indicate the signals expected for zero-valent Fe, mixed ferrous-ferric and pure ferric compounds, respectively. The N_{1s} XPS spectrum was fitted using eight individual spectral components that cover typical binding energy ranges of N species or motifs typically present in NC and MNC materials. The individual eight spectral component peaks were clustered into 4 BE-ranges. **BE-range 1** includes Peak 1 (398.1 eV) and Peak 2 (398.7 eV) covering N bonded to two sp^2-hybridized carbons and -C=N-C double bond motifs (e.g. Imine N, Pyridinic N or triazinic N). **BE-range 2** includes Peak 3 (399.3 eV) and Peak 4 (399.8 eV) covering sp^2 hybridized N in Metal-N coordination, OC-NH-C partial double bonds, or multiple graphitic N motifs in a single aromatic ring (e.g. M – Nx, Amides). **BE-range 3** includes Peak 5 (400.7 eV), Peak 6 (401.8 eV), and Peak 7 (403 eV) covering hybridized N bonded with 1 H (in-plane hydrogenated N), isolated graphitic N, out-of-plane hydrogenated/protonated N and hydrogenated graphitic N (e.g. pyrrolic or protonated pyridinic, protonated graphitic N). **BE-range 4** includes Peak 8 (405 eV) covering oxidized N (e.g. C=N-O or other oxidized N)[9, 10, 11, 12, 13, 14, 15]. The positions of the binding energies were chosen from DFT and experimental-DFT combinatorial studies on MNC and NC materials performed by Artyushkova *et al* [9, 10, 15, 16, 17, 18, 19, 20, 21].

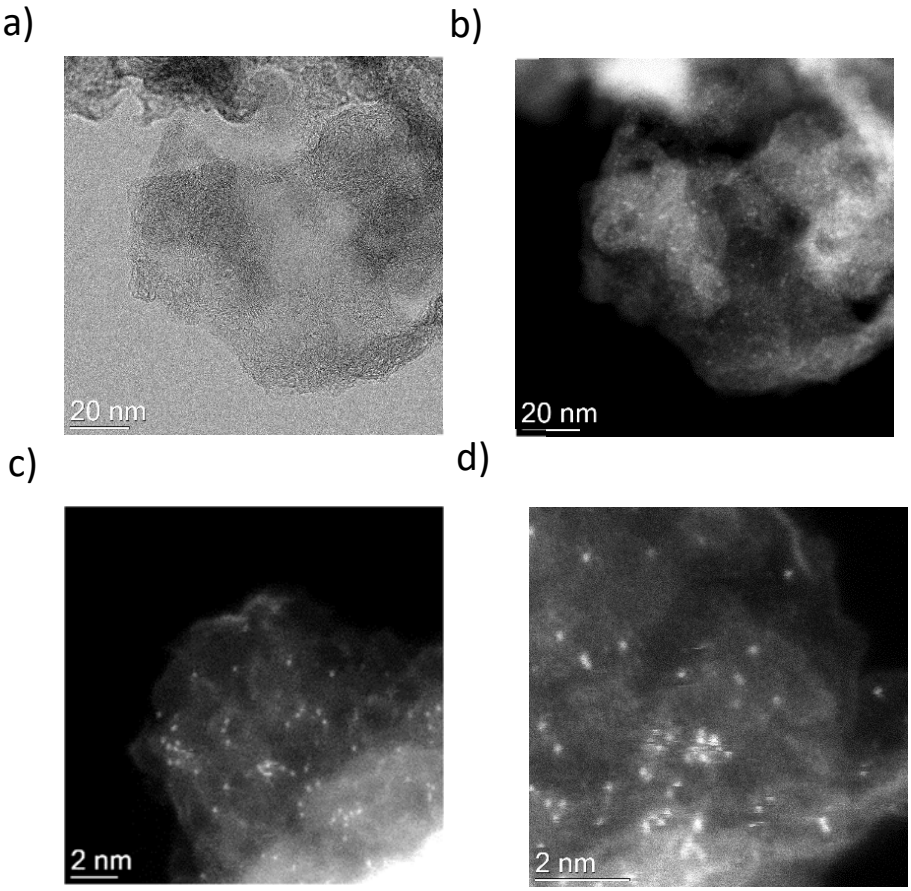

Figure S4. (a) Bright field STEM image of SnNC, (b) dark field STEM image of SnNC, (c) atomically-dispersed Sn atoms in the nitrogen-doped carbon matrix, (d) atomically dispersed Sn atoms in a more ordered graphene sheet.

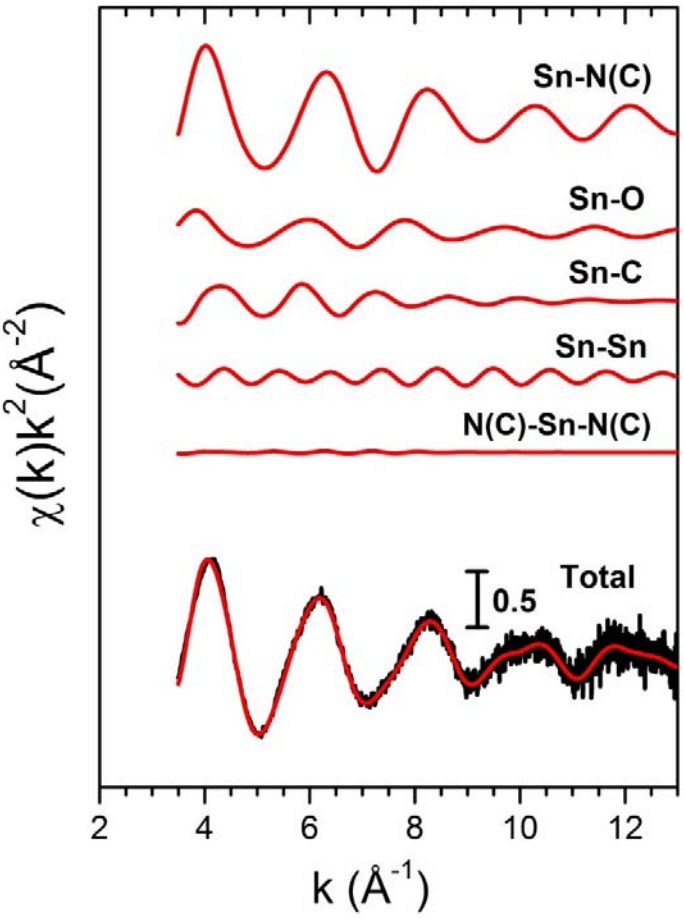

Figure S5. Sn K-edge EXAFS analysis of SnNC. Curves from top to bottom: Sn-N(C), Sn-O, Sn-C, Sn-Sn two-body signals, the N(C)-Sn-N(C) three body signal included in the fit, the total signal (red curve) superimposed to the experimental one (black curve). See the parameters resulting from the fitting in Table S4.

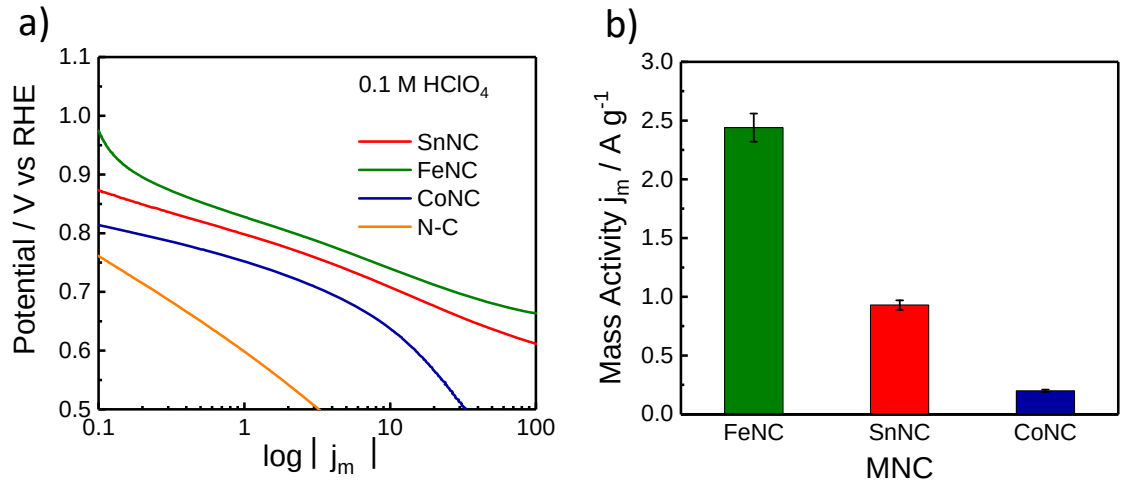

Figure S6. ORR mass activity of MNC catalysts as derived from RDE measurements. (a) Tafel plots and (b) mass activity for SnNC, FeNC and CoNC at 0.8 V *vs.* RHE. The kinetic Tafel plots and resulting catalyst mass activity, j_m, at 0.8 V_{RHE} after correction for O_2 diffusion (details in Supplementary Information) are compared.

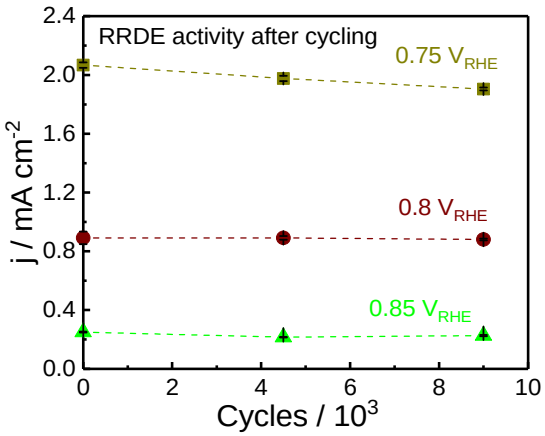

Figure S7. SnNC catalyst RRDE performance at various potentials after potential cycling in N_2 between 0.6 V_{RHE} and 1.0 V_{RHE} in 0.1M $HClO_4$ (catalyst loading, 0.8 mg cm^{-2}). Stability test protocols involved potential cycling within the cathode potential (RRDE) and voltage (fuel cell) range between 0.6 to 1.0 V in nitrogen in line with the widely accepted tests adopted by the U.S. automotive industry[22, 23].

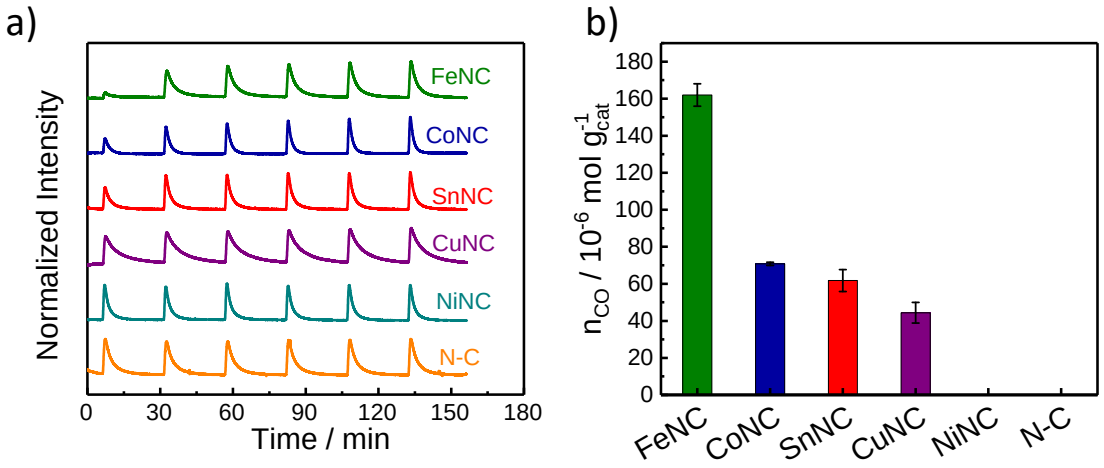

Figure S8. Quantification of the number of metal-based active sites with CO chemisorption. (a) CO pulse chemisorption profiles of NC (orange trace), NiNC (dark cyan trace), CuNC (purple trace), SnNC (red trace), CoNC (blue trace) and FeNC (olive trace) (b) CO uptake per mass of catalyst ($mol\ g_{cat}^{-1}$) as derived from the pulsed CO chemisorption profiles. The error is given in Table S5. Both on NiNC and N-C the CO chemisorption is below detection limit. This can explain the observed trend deviation in figure 3 of article main, where the DFT calculated activity underestimates the experimental value for NiNC, whose low currents detected could well be due to the N-C substrate instead.

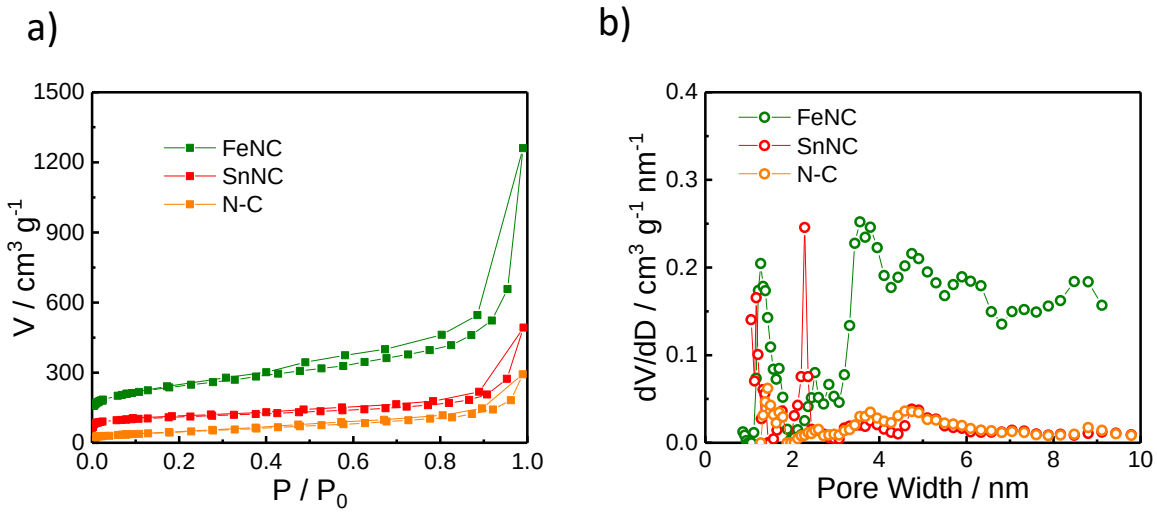

Figure S9. Carbon surface characterisation of FeNC, SnNC, and NC catalysts by N_2 physisorption. (a) Nitrogen sorption isotherms and (b) pore size distribution estimated from the adsorption branch by Non Localized Density Functional Theory with slit/cylindrical pore model.

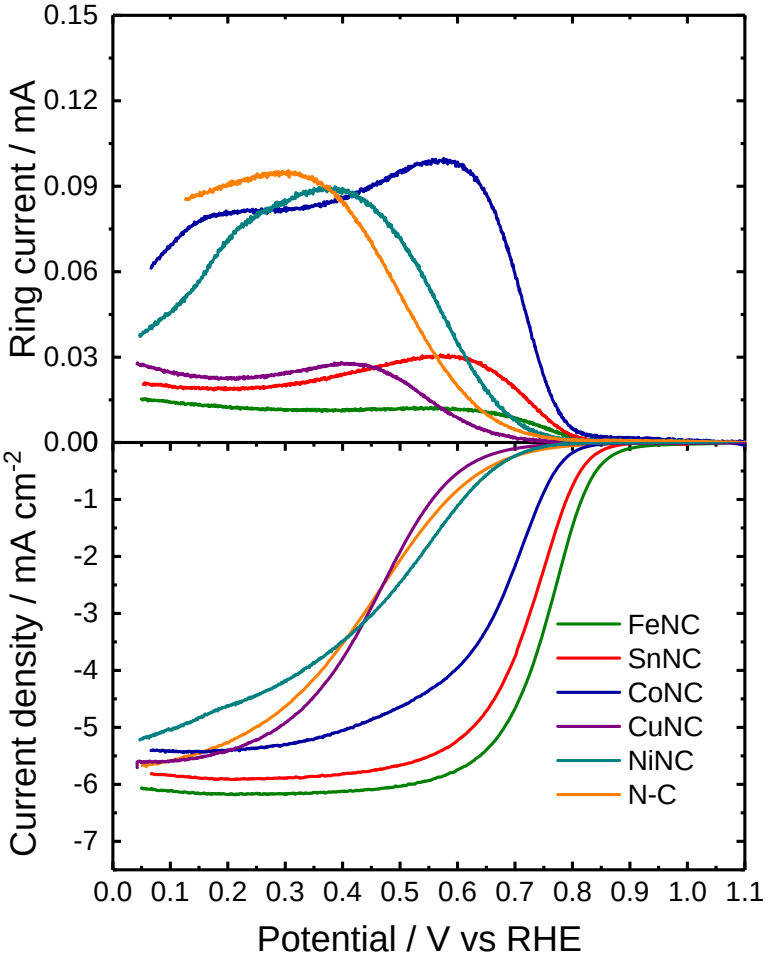

Figure S10. Electrochemical ORR activity and selectivity for MNC catalysts and NC. Steady-state ORR polarization curves and selectivity in O_2-saturated 0.1 M $HClO_4$ electrolyte. One slight mismatch between DFT theory and electrochemical ORR experiments is observed only for NiN_4C, the activity and selectivity of NiNC are however not significantly different from NC, suggesting negligible contribution from Ni sites. The absence of CO uptake on NiNC corroborates such a hypothesis (**Figure S8)**. These findings are in good agreement with earlier studies[18] and consistent with DFT studies on 3d transition-metal cations integrated in nitrogen-doped graphitic structures, that have shown weak O* adsorption energies on Ni and Cu[21].

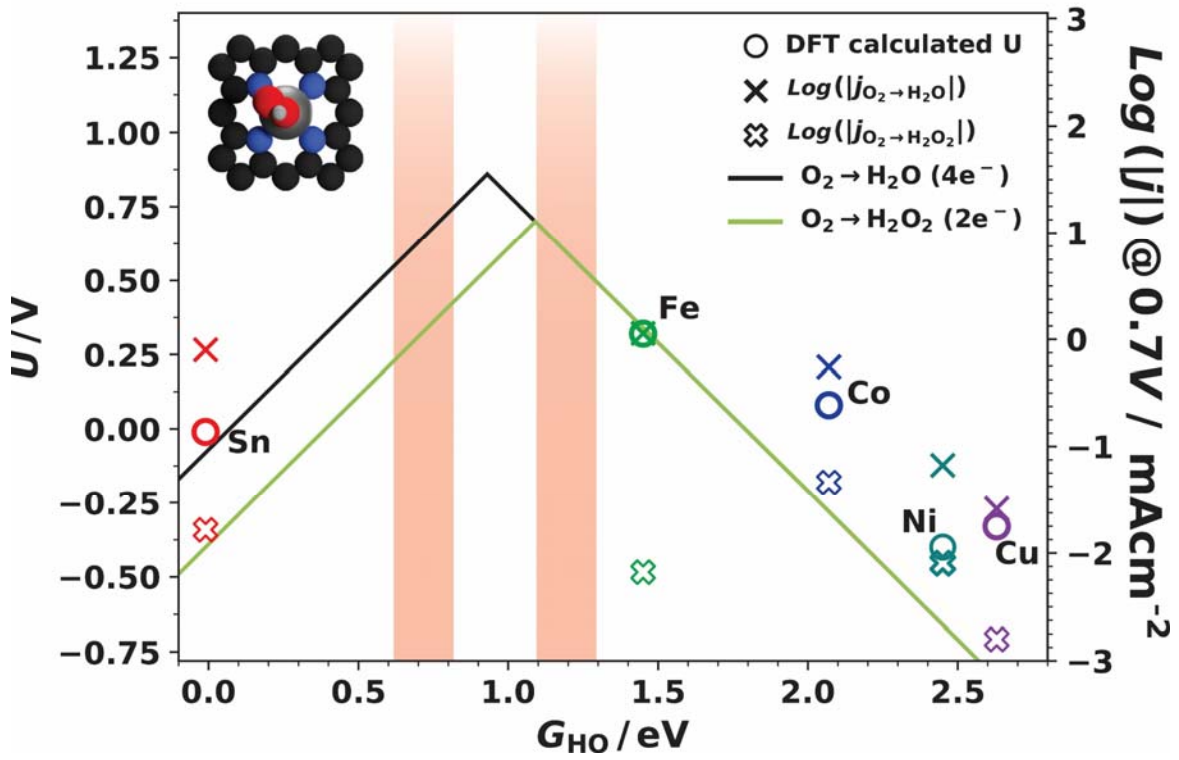

Figure S11. Volcano activity relationship for porphyrinic MN_4C motif (as in article main **Fig. 3 structure 8**) with M=Fe, Sn, Co, Cu and Ni. The experimental current densities when plotted versus the computed G_{HO} values for the porphyrinic motif outline a metal trend inconsistent with the volcano model for various reasons. First, active FeNC sites are considered strong binding limited, i.e. lying on the left volcano leg; second, all metals achieve only very low computed onset potentials; third, the higher J_{ring} measured on SnNC respect to FeNC is caused by weaker oxygen binding properties (i.e. a higher G_{HO} value) for SnNC than FeNC, opposite to what computed for porphyrinic MN_4C coordination. The porphyrinic motif is therefore deemed a worse approximation of the real catalytic site over the metal trend, as compared to the pyridinic motifs reported in **Fig. 3** in the article main.

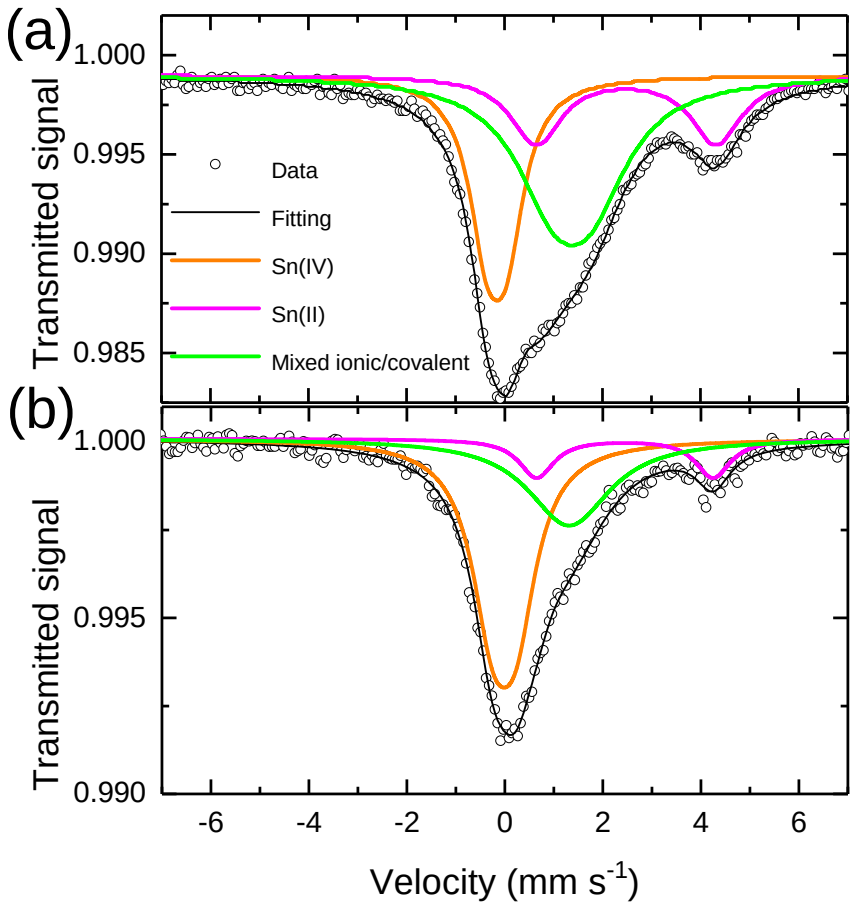

Figure S12. Alternative fitting strategy for ^{119}Sn Mössbauer spectroscopy characterization. (a) ^{119}Sn Mössbauer spectrum of SnNC and (b) ^{119}Sn Mössbauer spectrum of SnNC-NH_3. The spectra were measured at 300 K and the velocity scale was calibrated with $BaSnO_3$ at 300 K. The spectra were fitted with three spectral components and the Mössbauer parameters of each fitted component are reported in Table S10 and S11 for SnNC and SnNC-NH_3, respectively.

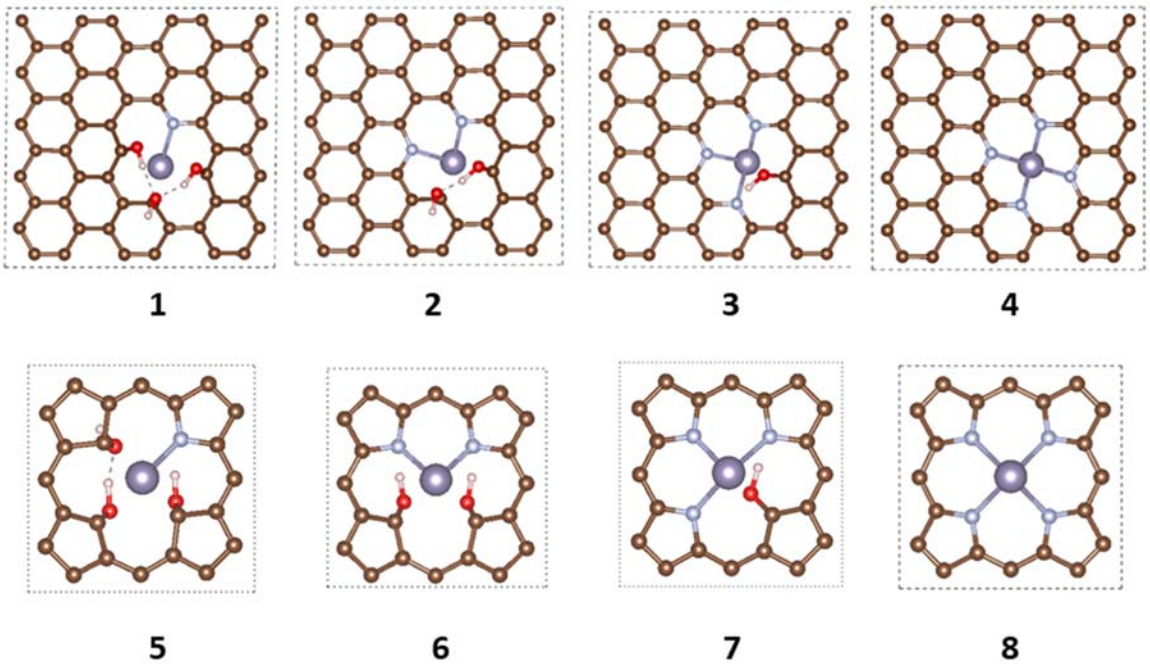

Figure S13. Geometries of the SnN_x structures for which the ΔE_{QS} values were calculated (no free O_2 present). Such a coordination is similar to those found in numerous metallo-enzymes. For example, FeN_4 in the planar porphyrin ring and CoN_4 in the nearly planar corrin ring (axial ligands are omitted) are the catalytic sites in cytochrome c oxidases[24, 25, 26] and vitamin B12[27], respectively, while non-planar Mn-N_3 is the catalytic site in manganese superoxide dismutase[28, 29]. Recent research has however shown that the integration of single metal cations in carbon matrices is possible even for Pt and Ru[30, 31, 32]. This highlights the potential for moving single-metal-atom sites beyond biomimicry, with no examples of metallo-enzymes involving such metals in nature[33, 34, 35].

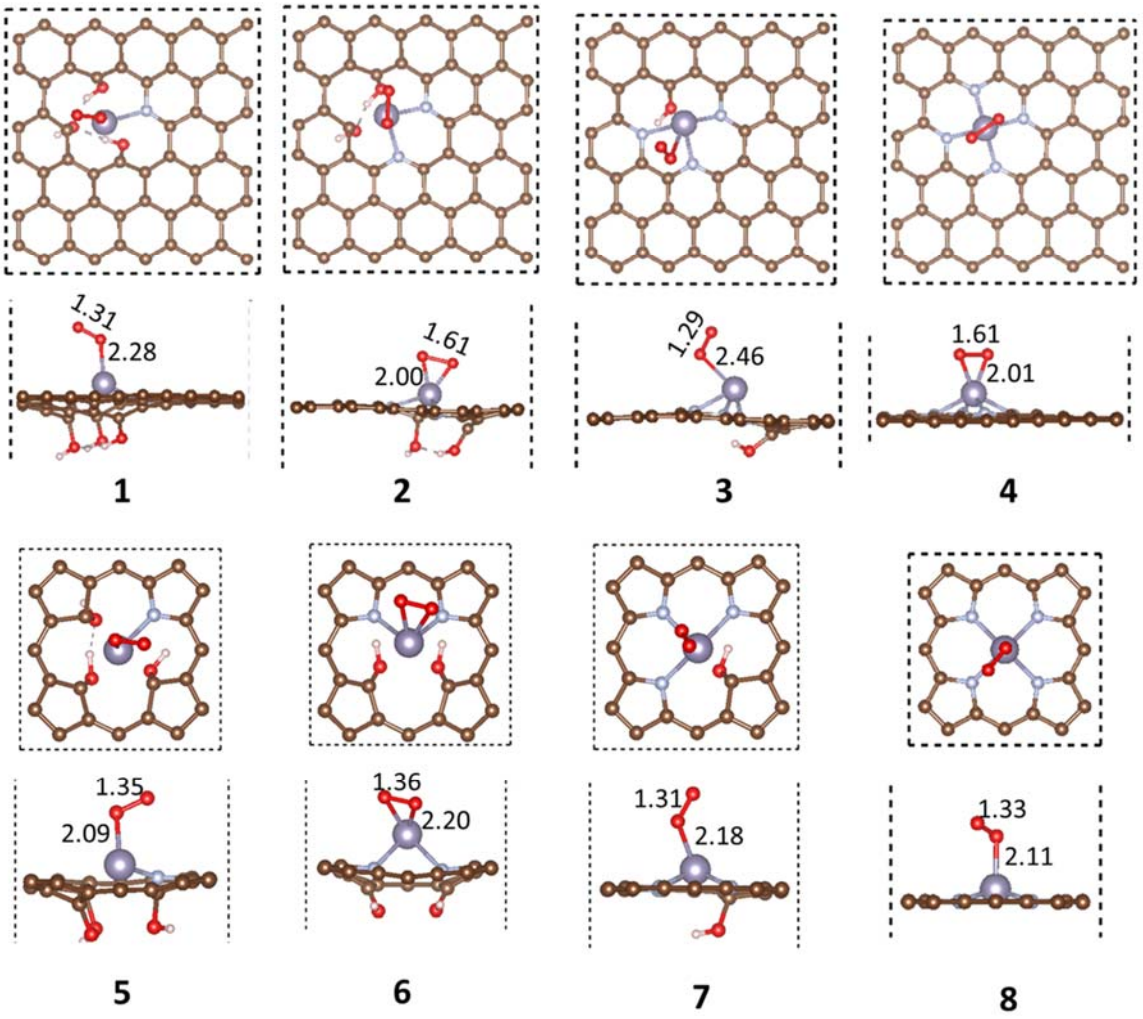

Figure S14. Geometries of the SnN_x structures for which the ΔE_{QS} values were calculated, after their relaxation upon approaching one O_2 molecule to the Sn center. The models show the Sn-O and O-O bonds and bond distances in Å.

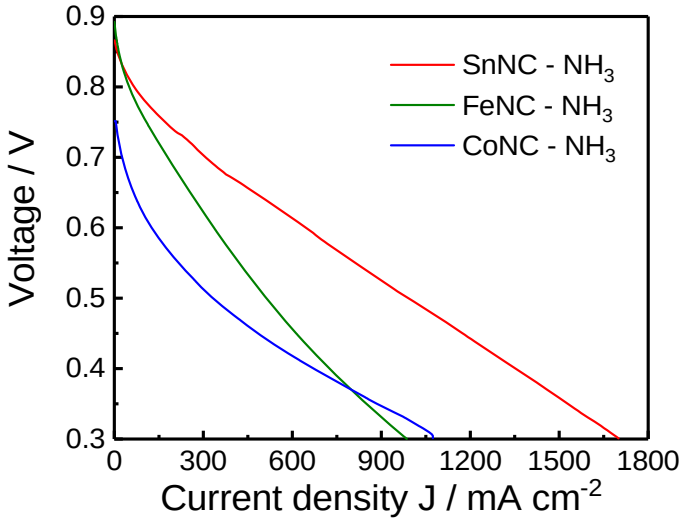

Figure S15. Fuel cell measurements. PEMFC polarization curves for SnNC, FeNC, and CoNC after NH_3 activation. The cathode loadings were 4 mg cm^{-2} with anode loadings of 2.0 mg_{Pt} cm^{-2}. Cell conditions: H_2-O_2 at 100% relative humidity (RH), $T_{anode} = T_{cathode} = 80$ ˚C at 2 bar absolute pressure. Polarization curves were acquired using linear sweep voltammetry with a sweep rate of $1mVs^{-1}$.

Table S1. Chemical composition of MNC and N-C, as measured by XPS.

	C / at %	N / at %	O / at %	Metal / at %
SnNC	91.9	5.0	2.8	0.3 (Sn)
FeNC	91.2	5.5	2.6	0.7 (Fe)
CoNC	90.8	5.2	3.6	0.4 (Co)
CuNC	93.0	5.6	1.1	0.3 (Cu)
NiNC	88.6	6.0	3.0	0.9 (Ni)
N-C	92.2	4.0	3.9	_

Table S2. Chemical composition of MNC and N-C, as measured by ICP and EA.

	Metal Content (ICP) / wt %	Nitrogen Content (EA) / wt %	Carbon Content (EA) / wt %	Sulfur Content (EA)/ wt%
SnNC	3.78	5.70	78.45	0.48
FeNC	3.92	6.43	76.41	0.96
CoNC	1.00	1.32	93.34	--
CuNC	2.87	8.95	81.86	0.01
NiNC	12.47	5.49	66.34	5.88
N-C	--	7.10	83.05	2.15

Table S3. Relative amount of nitrogen components, as obtained by fitting of the N_{1s} narrow scan XPS spectra to 8 individual N components. The latter were grouped into 4 distinct BE-ranges, due to recognized multiple possible assignment of nitrogen speciation in each of those BE ranges [15].

	BE- range 1 **N bonded to two sp^2 carbons, NC double bonds, -C=N-C** **(e.g. Imine, Pyridinic N, triazinic N)** **398-399 eV / at%**		**BE- range 2** **sp^2 N, N-Metal coordination, OC-NH-C, multiple graphitic N in a single aromatic ring** **(e.g. M – Nx, Amide)** **399 – 400 eV/ at%**		**BE- range 3** **in–plane hydrogenated N, isolated graphitic N, out-of-plane hydrogenated-N/protonated N, hydrogenated graphitic N** **(e.g. pyrrolic, protonated pyridinic)** **400 – 403 eV / at%**			**BE- range 4** **oxidized N (e.g. C=N-O) / at%**
BE	~398.1ev	~398.7ev	~399.3ev	~399.8ev	~400.7ev	~401.8ev	~403ev	~405ev
SnNC	21.2	9.7	6.5	4.4	46.8	8.3	2.3	0.8
FeNC	21.3	14.0	4.6	6.2	42.3	7.1	3.3	1.1
CoNC	17.7	23.8	8.0	2.3	35.9	5.7	6.2	0.5
CuNC	22.8	13.2	5.0	1.6	46.2	7.0	2.9	1.3
NiNC	8.7	21.3	5.6	1.5	48.9	7.7	5.0	1.4
N-C	25.3	0.4	6.4	2.5	52.7	8.5	2.6	1.6

Table S4. Best-fit parameters obtained from the EXAFS analysis of SnNC. R is the interatomic distance, σ^2 represents the Debye-Waller factor, and CN is the coordination number. Errors are given in parentheses, *e.g.* 2.06(1) means 2.05-2.07.

	R(Å)	**CN**	**σ^2(10^{-3} Å2)**
Sn-N(C)	2.06(1)	3.9(3)	5.8(3)
Sn-O	2.13(2)	1.0(2)	2.8(7)
Sn-C	2.73(1)	4.7(5)	10.0(1)
Sn-Sn	3.28(1)	1.0(2)	7.6(4)

Table S5. Results of CO pulse chemisorption experiments. Measurements were repeated five times for each catalyst, from which the experimental error was derived. The table below indicates the average nCO value and the standard error for each catalyst.

Catalyst	FeNC	SnNC	CoNC	CuNC	NiNC	NC
n_{CO} / 10^{-6} mol g^{-1}	162.00	61.77	70.80	44.40	0.00	0.00
Error / 10^{-6} mol g^{-1}	6.08	4.15	0.84	5.55	0.00	0.00

Table S6. Turn over Frequency (TOF) values at 0.8 V vs. RHE in pH 1 electrolyte for the MNC catalysts.

Catalyst	**FeNC**	**SnNC**	**CoNC**	**CuNC**
TOF / electrons site^{-1} s^{-1}	0.156	0.155	0.029	0.006

Table S7. Pore size characterization for the MNC and N-C catalysts.

	Micropore volume / cm^3 g^{-1}	**Mesopore volume / cm^3 g^{-1}**	**Micropore Surface Area / m^2 g^{-1}**	**BET Surface Area / m^2 g^{-1}**
SnNC	0.11	0.21	314	364
FeNC	0.20	0.45	587	665
NC	0.02	0.20	47	174

Table S8. Disk current and ring current at 0.7 V *vs.* RHE from RRDE experiments for MNC catalysts. The experiments were performed in 0.1 M $HClO_4$ electrolyte.

	Disk current / mA	**Ring current / mA**	**H_2O_2 / %**
SnNC	-0.80±0.04	0.017±0.002	10.7±1.1
FeNC	-1.14±0.03	0.007±0.0002	2.8±0.1
CoNC	-0.55±0.01	0.049±0.004	39.4±2.8
CuNC	-0.03±0.002	0.002±0.0002	28.0±2.3
NiNC	-0.07±0.01	0.008±0.0004	49.9±4.4

Table S9. Parameters of the spectral components obtained from the fitting of the ^{119}Sn Mössbauer spectrum for SnNC (Figure 4). The spectrum was measured at 300 K, and IS values are referred to $BaSnO_3$, with absorber and source at 300 K. While another mathematically possible fitting approach was initially identified for SnNC, involving a quadrupole doublet component with high QS-value of ca 3.7 mm/s and IS of 2.5 mm/S, there is presently no theoretical support for the existence of an atomically dispersed Sn moiety with such high QS-value. The fitting strategy reported in Figure 4 and Table S9 was thus preferred. This choice was based on: a) the fact that all the DFT-calculated QS-values of Sn-N_x moieties are well below 3.7 mm/s (Table S13), while the QS-values for the Sn(II)-a and Sn(II)-b components (2.41 and 1.24 mm/s) of the adopted fitting strategy are well in line with the QS-values calculated by DFT for the structures 1-8 (Table S13).

	Sn(IV)-a	**Sn(IV)-b**	**Mixed ionic/covalent**	**Sn(II)-a**	**Sn(II)-b**
IS / mm s^{-1}	-0.05	-0.13	1.26	3.29	3.29
QS / mm s^{-1}	0.97	-	0.50	2.41	1.24
Γ / mm s^{-1}	0.93	0.93	1.00	1.08	0.98
Area / %	26	24	25	17	8
Oxidation State	Sn(IV)	Sn(IV)	Mixed ionic/covalent	Sn(II)	Sn(II)

Table S10. Parameters of the spectral components obtained from the alternative fitting of the ^{119}Sn Mössbauer spectrum for SnNC.

	Sn(IV)-a	**Mixed ionic/covalent**	**Sn(II)-a**
IS / mm s^{-1}	-0.16	1.38	2.49
QS / mm s^{-1}	0.41	0.77	3.67
Γ / mm s^{-1}	0.87	1.89	1.25
Area / %	30.6	47.7	21.7
Oxidation State	Sn(IV)	Mixed ionic/covalent	Sn(II)

Table S11. Parameters of the spectral components obtained from the alternative fitting of the ^{119}Sn Mössbauer spectrum for SnNC-NH_3.

	Sn(IV)-a	**Mixed ionic/covalent**	**Sn(II)-a**
IS / mm s^{-1}	-0.015	1.31	2.45
QS / mm s^{-1}	0.48	0.26	3.60
Γ / mm s^{-1}	1.04	1.97	0.86
Area / %	56.6	31.4	12.0
Oxidation State	Sn(IV)	Mixed ionic/covalent	Sn(II)

Table S12. Elemental composition (at.%=atomic percentage) from EDS quantification of HAADF-STEM.

SnNC	Area 1 (at.%)	Area 2 (at.%)	Area 3 (at.%)	Average (at.%)
C	93.05	92.84	92.99	**92.96**
N	4.23	4.46	4.47	**4.39**
O	2.23	2.22	2.06	**2.17**
Na	0.07	0.09	0.07	**0.08**
S	0.17	0.16	0.15	**0.16**
Fe	0.03	0.03	0.02	**0.03**
Sn	0.22	0.20	0.22	**0.21**

Table S13. Calculated QS values for the structures 1-8, without and with O_2 adsorbed on the structures. The geometries of the structures optimized for QS calculation are shown in Figure S13-S14.

Structure Nbr.	**QS / mm s^{-1}**	
	Without oxygen	With oxygen adsorbed
1	2.6	1.1
2	2.7	1.2
3	2.0	1.5
4	1.6	1.0
5	2.4	1.5
6	2.7	1.5
7	2.4	1.4
8	0.9	0.9

Table S14. Parameters of the spectral components obtained from the fitting of the ^{119}Sn Mössbauer spectrum for SnNC-NH_3. The spectrum was measured at 300 K, and IS values are referred to $BaSnO_3$, with absorber and source at 300 K. Due to the possibility of very different Lamb Mössbauer factors for different Sn coordinations at 300 K, the area % are not necessarily representative of the true relative % of each Sn species.

	Sn(IV)-a	**Sn(IV)-b**	**Mixed ionic/covalent**	**Sn(II)-a**	**Sn(II)-b**
IS / mm s^{-1}	0.01	-0.02	1.44	3.47	2.85
QS / mm s^{-1}	0.90	-	0.59	1.51	2.83
Γ / mm s^{-1}	1.04	1.04	0.92	1.03	0.92
Area / %	42	32	12	6	8
Oxidation State	Sn(IV)	Sn(IV)	Mixed ionic/covalent	Sn(II)	Sn(II)

Table S15. The comparison for ORR performances in half-cell and fuel cell condition. The SnNCcatalyst exhibits comparable performance to other catalyst types previously reported FeNC or CoNC under similar conditions, including compared MEA performance with a state-of-the-art Pt/C catalyst[36, 37, 38, 39, 40].

Catalysts	ORR Electrolyte	Half-wave potential $E_{1/2}$ V_{RHE}	PEMFC conditions	PEMFC Kinetic region of cathode
FeNC[36]	0.5 M H_2SO_4	0.8	1.0 bar H_2-O_2 Cathode loading:4 mg cm^{-2}	~ 0.75 V
FeNC[37]	0.5 M H_2SO_4	0.88	1.0 bar H_2-O_2 Cathode loading:4 mg cm^{-2}	~ 0.8 V
FeNC-2[38]	0.5 M H_2SO_4	0.71	-	-
50 wt % Pt/C ($0.1mg_{pt}$ cm^{-2}) [36]	-	-	1.0 bar H_2-O_2 Cathode loading: $0.1mg_{pt}$ cm^{-2}	~ 0.75 V
Commercial Pt/C[39]	0.1 M $HClO_4$	0.86	-	-
CoNC[40]	0.1 M $HClO_4$	0.72	-	-
FeNC(This work)	0.1 M $HClO_4$	0.79	2.0 bar H_2-O_2 Cathode loading:4 mg cm^{-2}	~ 0.7 V
SnNC(This work)	0.1 M $HClO_4$	0.73	2.0 bar H_2-O_2 Cathode loading:4 mg cm^{-2}	~ 0.75 V

Supporting references

1. Jaouen F, Lefèvre M, Dodelet J-P, Cai M. Heat-Treated Fe/N/C Catalysts for O2 Electroreduction: Are Active Sites Hosted in Micropores? *The Journal of Physical Chemistry B* 2006, **110**(11)**:** 5553-5558.

2. Knop‐Gericke A, Kleimenov E, Hävecker M, Blume R, Teschner D, Zafeiratos S*, et al.* Chapter 4 X‐Ray Photoelectron Spectroscopy for Investigation of Heterogeneous Catalytic Processes. *Advances in Catalysis*, vol. 52. Academic Press, 2009, pp 213-272.

3. Filipponi A, Di Cicco A, Natoli CR. X-ray-absorption spectroscopy and n-body distribution functions in condensed matter. I. Theory. *Physical Review B* 1995, **52**(21)**:** 15122-15134.

4. Filipponi A, Di Cicco A. X-ray-absorption spectroscopy and n-body distribution functions in condensed matter. II. Data analysis and applications. *Physical Review B* 1995, **52**(21)**:** 15135-15149.

5. Luo F, Choi CH, Primbs MJM, Ju W, Li S, Leonard ND*, et al.* Accurate Evaluation of Active-Site Density (SD) and Turnover Frequency (TOF) of PGM-Free Metal–Nitrogen-Doped Carbon (MNC) Electrocatalysts using CO Cryo Adsorption. *ACS Catalysis* 2019**:** 4841-4852.

6. Mineva T, Matanovic I, Atanassov P, Sougrati M-T, Stievano L, Clémancey M*, et al.* Understanding Active Sites in Pyrolyzed Fe–N–C Catalysts for Fuel Cell Cathodes by Bridging Density Functional Theory Calculations and 57Fe Mössbauer Spectroscopy. *ACS Catalysis* 2019, **9**(10)**:** 9359-9371.

7. Davis SR, Chadwick AV, Wright JD. A Combined EXAFS and Diffraction Study of Pure and Doped Nanocrystalline Tin Oxide. *The Journal of Physical Chemistry B* 1997, **101**(48)**:** 9901-9908.

8. Zitolo A, Ranjbar-Sahraie N, Mineva T, Li J, Jia Q, Stamatin S*, et al.* Identification of catalytic sites in cobalt-nitrogen-carbon materials for the oxygen reduction reaction. *Nature Communications* 2017, **8**(1)**:** 957.

9. Artyushkova K, Kiefer B, Halevi B, Knop-Gericke A, Schlogl R, Atanassov P. Density functional theory calculations of XPS binding energy shift for nitrogen-containing graphene-like structures. *Chem Commun (Camb)* 2013, **49**(25)**:** 2539-2541.

10. Artyushkova K, Serov A, Rojas-Carbonell S, Atanassov P. Chemistry of Multitudinous Active Sites for Oxygen Reduction Reaction in Transition Metal–Nitrogen–Carbon Electrocatalysts. *The Journal of Physical Chemistry C* 2015, **119**(46)**:** 25917-25928.

11. Kattel S, Atanassov P, Kiefer B. Density Functional Theory Study of Ni–Nx/C Electrocatalyst for Oxygen Reduction in Alkaline and Acidic Media. *The Journal of Physical Chemistry C* 2012, **116**(33)**:** 17378-17383.

12. Kattel S, Atanassov P, Kiefer B. Catalytic activity of Co-N(x)/C electrocatalysts for oxygen reduction reaction: a density functional theory study. *Physical chemistry chemical physics : PCCP* 2013, **15**(1)**:** 148-153.

13. Kattel S, Atanassov P, Kiefer B. A density functional theory study of oxygen reduction reaction on non-PGM Fe-Nx-C electrocatalysts. *Physical chemistry chemical physics : PCCP* 2014, **16**(27)**:** 13800-13806.

14. Qian Y, Du P, Wu P, Cai C, Gervasio DF. Chemical Nature of Catalytic Active Sites for the Oxygen Reduction Reaction on Nitrogen-Doped Carbon-Supported Non-Noble Metal Catalysts. *The Journal of Physical Chemistry C* 2016, **120**(18)**:** 9884-9896.

15. Artyushkova K. Misconceptions in interpretation of nitrogen chemistry from x-ray photoelectron spectra. *Journal of Vacuum Science & Technology A* 2020, **38**(3)**:** 031002.

16. Guo D, Shibuya R, Akiba C, Saji S, Kondo T, Nakamura J. Active sites of nitrogen-doped carbon materials for oxygen reduction reaction clarified using model catalysts. *Science* 2016, **351**(6271)**:** 361-365.

17. Herranz J, Jaouen F, Lefèvre M, Kramm UI, Proietti E, Dodelet J-P*, et al.* Unveiling N-Protonation and Anion-Binding Effects on Fe/N/C Catalysts for O2 Reduction in Proton-Exchange-Membrane Fuel Cells. *The Journal of Physical Chemistry C* 2011, **115**(32)**:** 16087-16097.

18. Sahraie NR, Kramm UI, Steinberg J, Zhang Y, Thomas A, Reier T*, et al.* Quantifying the density and utilization of active sites in non-precious metal oxygen electroreduction catalysts. *Nat Commun* 2015, **6:** 8618.

19. Vayner E, Anderson AB. Theoretical Predictions Concerning Oxygen Reduction on Nitrided Graphite Edges and a Cobalt Center Bonded to Them. *The Journal of Physical Chemistry C* 2007, **111**(26)**:** 9330-9336.

20. Masa J, Xia W, Muhler M, Schuhmann W. On the Role of Metals in Nitrogen-Doped Carbon Electrocatalysts for Oxygen Reduction. *Angewandte Chemie* 2015, **54**(35)**:** 10102-10120.

21. Calle-Vallejo F, Martinez JI, Rossmeisl J. Density functional studies of functionalized graphitic materials with late transition metals for Oxygen Reduction Reactions. *Physical chemistry chemical physics : PCCP* 2011, **13**(34)**:** 15639-15643.

22. Schmies H, Hornberger E, Anke B, Jurzinsky T, Nong HN, Dionigi F*, et al.* Impact of Carbon Support Functionalization on the Electrochemical Stability of Pt Fuel Cell Catalysts. *Chemistry of Materials* 2018, **30**(20)**:** 7287-7295.

23. Atsushi Ohmaa KS, Akihiro Iiyamaa,Toshihiko Yoshidab and Akimasa Daimaru. Membrane and Catalyst Performance Targets for Automotive Fuel Cells by FCCJ Membrane, Catalyst, MEA WG. *ECS Transactions* 2011, **41**(1).

24. Blomberg MRA. Mechanism of Oxygen Reduction in Cytochrome c Oxidase and the Role of the Active Site Tyrosine. *Biochemistry* 2016, **55**(3)**:** 489-500.

25. Ferguson-Miller S, Babcock GT. Heme/Copper Terminal Oxidases. *Chemical Reviews* 1996, **96**(7)**:** 2889-2908.

26. Yoshikawa S, Shinzawa-Itoh K, Nakashima R, Yaono R, Yamashita E, Inoue N*, et al.* Redox-Coupled Crystal Structural Changes in Bovine Heart Cytochrome c Oxidase. *Science* 1998, **280**(5370)**:** 1723-1729.

27. Hodgkin DC, Kamper J, Mackay M, Pickworth J, Trueblood KN, White JG. Structure of Vitamin B12. *Nature* 1956, **178**(4524)**:** 64-66.

28. Borgstahl GEO, Pokross M, Chehab R, Sekher A, Snell EH. Cryo-trapping the six-coordinate, distorted-octahedral active site of manganese superoxide dismutase11Edited by R. Huber. *Journal of Molecular Biology* 2000, **296**(4)**:** 951-959.

29. Azadmanesh J, Borgstahl GEO. A Review of the Catalytic Mechanism of Human Manganese Superoxide Dismutase. *Antioxidants* 2018, **7**(2)**:** 25.

30. Yao Y, Huang Z, Xie P, Wu L, Ma L, Li T*, et al.* High temperature shockwave stabilized single atoms. *Nature nanotechnology* 2019, **14**(9)**:** 851-857.

31. Liu J, Jiao M, Lu L, Barkholtz HM, Li Y, Wang Y*, et al.* High performance platinum single atom electrocatalyst for oxygen reduction reaction. *Nat Commun* 2017, **8:** 15938.

32. Ott S, Orfanidi A, Schmies H, Anke B, Nong HN, Hübner J*, et al.* Ionomer distribution control in porous carbon-supported catalyst layers for high-power and low Pt-loaded proton exchange membrane fuel cells. *Nature materials* 2019.

33. Waldron KJ, Rutherford JC, Ford D, Robinson NJ. Metalloproteins and metal sensing. *Nature* 2009, **460**(7257)**:** 823-830.

34. Yannone SM, Hartung S, Menon AL, Adams MWW, Tainer JA. Metals in biology: defining metalloproteomes. *Current Opinion in Biotechnology* 2012, **23**(1)**:** 89-95.

35. Cvetkovic A, Menon AL, Thorgersen MP, Scott JW, Poole Ii FL, Jenney Jr FE*, et al.* Microbial metalloproteomes are largely uncharacterized. *Nature* 2010, **466**(7307)**:** 779-782.

36. Chung HT, Cullen DA, Higgins D, Sneed BT, Holby EF, More KL*, et al.* Direct atomic-level insight into the active sites of a high-performance PGM-free ORR catalyst. *Science* 2017, **357**(6350)**:** 479-484.

37. Zhang H, Chung HT, Cullen DA, Wagner S, Kramm UI, More KL*, et al.* High-performance fuel cell cathodes exclusively containing atomically dispersed iron active sites. *Energy & Environmental Science* 2019, **12**(8)**:** 2548-2558.

38. Mathias Primbs PS, Deborah Jones, Frederic Jaouen, Aaron Roy, Pierre-Yves Blanchard, Moulay Tahar Sougrati, Daniel Malko, Anthony Kucernak, Gaetano Granozzi, Christian Durante, Tomasz Kosmala, Valentina Perazzolo, Jonathan Sharman. CRESCENDO Deliverable Report D3.1-Site Density and Turn over frequency of selected benchmark catalysts. http://www.crescendo-fuelcell.eu/index.php/activities/deliverables?jjj=1565098846810; 2018, 05.

39. Li M, Zhao Z, Cheng T, Fortunelli A, Chen C-Y, Yu R*, et al.* Ultrafine jagged platinum nanowires enable ultrahigh mass activity for the oxygen reduction reaction. *Science* 2016, **354**(6318)**:** 1414-1419.

40. Wu G, More KL, Johnston CM, Zelenay P. High-Performance Electrocatalysts for Oxygen Reduction Derived from Polyaniline, Iron, and Cobalt. *Science* 2011, **332**(6028)**:** 443-447.